FTIR Adsorption Studies of H_2O and CH_3OH in the Isostructural H-SSZ-13 and H-SAPO-34: Formation of H-Bonded Adducts and Protonated Clusters

Silvia Bordiga, Laura Regli, Carlo Lamberti, and Adriano Zecchina*

Dipartimento di Chimica IFM and NIS Centre of Excellence, Via P. Giuria 7, I-10125 Torino, Italy

Morten Bjørgen and Karl Petter Lillerud

Department of Chemistry, University of Oslo, P.O. Box 1033, N-0315 Oslo, Norway

Received: December 13, 2004; In Final Form: February 14, 2005

The acidity of the isostructural H-SSZ-13 and H-SAPO-34 has been investigated by transmission FTIR spectroscopy using H_2O and CH_3OH as molecular probes. Interactions between the zeolitic samples and the probe molecules led to perturbations and proton transfers directly related to the acidity of the materials. The entire set of acidic sites in H-SSZ-13 interacts with H_2O and CH_3OH to give H-bonded adducts or protonated species. H_3O^+ is not formed in appreciable amounts upon H_2O adsorption on H-SSZ-13, but at high coverages H_2O generates clusters that have a proton affinity sufficiently high to abstract protons from the zeolite framework. Parallel experiments carried out for H-SAPO-34 showed that the H_2O clusters abstract protons from Brønsted sites only to a minor extent. Moving to CH_3OH, even if it has a higher proton affinity than H_2O and should expectingly experience an easier protonation, proton transfer is totally absent in H-SAPO-34 under our set of conditions. The clear evidence of methanol protonation in H-SSZ-13 definitely states the strong acidic character of this material. When irreversibly adsorbed CH_3OH is present in H-SSZ-13, an appreciable amount of $(CH_3)_2O$ is formed upon heating to 573 K. Compared to its SAPO analogue, the present set of data indisputably points to H-SSZ-13 as the strongest Brønsted acidic material.

1. Introduction

A great number of industrial processes rely on heterogeneous catalysis. The majority of these processes are of vital importance to our present-day standard of living, but yet more efficient catalysts are desirable. This work is devoted to protonated zeolites, a class of catalytic materials widely employed in, for example, the petrochemical industry. For protonated zeolites, the acidity, along with the nanopore topology, is determinant for catalyst activity and selectivity. Indeed, when aiming at developing more favorable zeolite catalysts, the intrinsic properties of the materials should be understood in more detail.

Zeolite and zeotype materials having the chabazite topology, such as H-SAPO-34, are particularly promising for the reaction where CH_3OH is converted into H_2O and a mixture of light olefins (MTO).[1−4] When CH_3OH is introduced into a protonated zeolite at elevated temperatures, the equlibrium between CH_3OH, dimethyl ether ($(CH_3)_2O$), and H_2O will readily establish. After an induction period, hydrocarbon formation will take place. Under operating conditions, the main reaction path for hydrocarbon formation from CH_3OH appears to be the so-called hydrocarbon pool mechanism.[5] A crucial point for understanding the activation and the initial reactions of CH_3OH in protonated zeolitic materials is the nature of the adsorbed complex. The focus of the main debate has been to answer whether CH_3OH is adsorbed as a neutral hydrogen-bonded complex or if proton transfer occurs and forms an ion pair. A further interesting point is the possible difference between H-SAPO-34 and its zeolitic homologue H-SSZ-13 (a chabazite variant with a rather low aluminum content and thus a relatively low density of acidic sites). Thus far, direct comparisons between these two materials have been funded on molecular modeling, presumably because of the difficulties in obtaining H-SSZ-13.[6−9] H-ZSM-5 and some other zeolites with a low Al content have been used as term of paragon in respect of H-SAPO-34.[10,11] In this contribution, we provide a directly comparable set of data describing the interactions between both H_2O and CH_3OH and H-SSZ-13/H-SAPO-34.

Very recently, we presented a work where CO adsorption studies allowed us to comprehend the distribution of the protons in H-SSZ-13 at a more detailed level.[12] It appears likely that the Brønsted sites of H-SSZ-13 are constituted by two families, one having an IR stretching frequency at 3616 cm^{-1} (HF) and the other at 3584 cm^{-1} (LF).[12] In addition to showing distinct IR frequencies, it is also rather evident that the sites belonging to the HF family is more accessible to probe molecules such as CO. On the basis of the CO experiments, the acidity of the two families seems to be rather similar. That data suggested that the LF band represents the only site (among four possible) not directly exposed to the eight-ring window. The remaining protons, all located in a highly exposed position on the eight-ring windows, contribute to the HF band. At least at temperatures above 77 K, it appears essential to consider proton distributions among all four sites. The data obtained for H-SSZ-13 were compared with parallel measurements on H-SAPO-34. Rather small differences were found, but a slightly weaker acidity was suggested for H-SAPO-34. The chabazite topology has been described thoroughly in previous reports,[12] and only the main features are summarized here. The chabazite lattice is composed of layers of double six rings that are interconnected by four rings, leading to a regular arrangement of barrel-shaped

* Author to whom correspondence should be addressed.

10.1021/jp044324b CCC: $30.25
Published on Web 04/06/2005

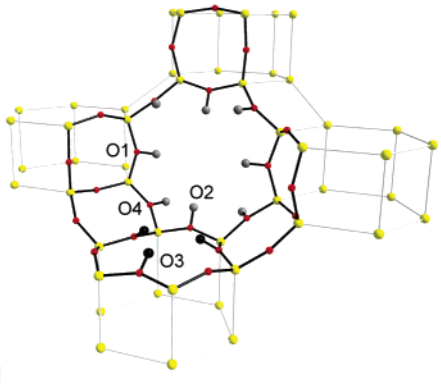

Figure 1. Schematic drawing of the chabazite framework. The black bold part of the framework shows one eight-ring window and one of the six rings with the four proton positions. Symmetry equivalent positions cause the sites to be represented with two, three, or four protons. Protons attached to O(3) (black) are not exposed to the eight-ring window and are thus distinctive from those attached to O(1), O(2), and O(4) (grey).

cages. The cages will be accessible through eight-ring windows. The chabazite structure provides four possible acid site configurations, depending on to which oxygen atom the proton is attached. Previously introduced designations of the proton positions[13] are adopted in this work as illustrated in Figure 1.

2. Experimental

The H-SAPO-34 sample was synthesized and calcined in accordance with standard procedures.[14] Zeolite SSZ-13 was obtained from a hydrothermal synthesis described elsewhere.[15] The acidic form of SSZ-13 was obtained by a carefully controlled calcination procedure described in ref 12, where also details concerning the physical characterization were provided. The Si/Al ratio of the H-SSZ-13 sample is 11.6, while the Si content of the H-SAPO-34 material has been chosen to result in an equal density of acidic sites. FTIR transmission spectra were collected in a controlled atmosphere using compressed self-supporting zeolite wafers. The samples were pretreated in situ under high vacuum at temperatures up to 773 K. H_2O and CH_3OH were dosed from an online vacuum rig and the spectra were recorded at 2 cm^{-1} resolution on a Bruker IFS 66 FTIR spectrometer, equipped with an MCT detector.

3. Results and Discussion

3.1 H_2O as Base for Probing the Acidity of H-SSZ-13 and H-SAPO-34 by FTIR. To obtain a more detailed insight into the acidity of H-SSZ-13, H_2O adsorption studies were carried out. H_2O adsorption on protonated zeolites has attracted considerable attention in the past decade and touches one of the most fundamental aspects in zeolite catalysis, namely, zeolite acidity and proton transfer to adsorbed species. H_2O adsorption on Brønsted acidic zeolites in general involves several rather complex phenomena. An overview of the different aspects of this topic is therefore included.

3.1.1 H_2O Adsorption on Protonated Zeolites. General Considerations. Both experimental[16−25] and theoretical[26−33] methods have been exploited to achieve insight into the specifics of the interaction between H_2O and Brønsted sites of zeolites. It now appears that a general agreement about the description of main features has been achieved. A key point which has been established is that the proton affinity of single H_2O molecules (PA = 166.5 kcal mol^{-1}) is not the only parameter that should be considered when evaluating the presence of neutral or protonated adsorbed species. An important point is the ratio between adsorbed H_2O molecules and Brønsted sites: When this ratio is >1, H_2O is in excess; cooperative effects start to play an important role and some relevant changes can be observed.

Among experimental techniques, infrared spectroscopy has been extensively used to study this subject as vibrational properties of H_2O and hydronium ions are well-known and as the formation of medium-strong H-bonds have peculiar infrared features.

The early experiments based on infrared spectroscopy underlined the formation of a doublet at about 2885 and 2463 cm^{-1} which was assigned to symmetric and asymmetric stretching modes of hydronium ions. This first assignment was reconsidered when it was observed that at higher H_2O coverages the spectra underwent much more complex changes. In particular, it has been observed that H_2O adsorption on protonic zeolites is accompanied by a growth of a triplet, denoted the *ABC* triplet (see Figure 8c, d in the Appendix).[19] The nature of this triplet has been described in previous works and only a very short analysis will be given here. The *A*, *B*, and *C* bands are normally located at 3000−2870, 2515−2400, and 1700 cm^{-1}, respectively. At low H_2O coverages, two additional evident peaks, around 3700 and 3550 cm^{-1}, are usually observed.

The idea that single H_2O molecules are able to deprotonate Brønsted sites in zeolites forming H_3O^+ species was first questioned by van Santen and co-workers,[26] who concluded that neutral species are more stable than protonated. Moreover, experiments involving ^{18}O-labeled H_2O molecules have conclusively led to an assignment of the *AB* bands to H-bonded ($_{zeolite}OH\cdots O_{water}$) complexes, and their relation to hydronium ions was thus disproven.[18,23] The isotopic shifts of other bands also confirmed the features expected for a H-bonded model. Very recently, Mihaleva et al. calculated the frequencies of the OH groups in chabazite in the presence of H_2O using anharmonic potential energy and dipole surfaces constructed from the zeolite OH stretch, in-plane bending (δ), out-of-plane bending (γ), and the H_2O molecule center of mass.[34] The experimentally observed *ABC* triplet fit well with OH vibrations in ($_{zeolite}OH\cdots O_{water}$) H-bonded complexes. Other quantum chemical studies have also found H-bonded H_2O, and not protonated H_2O, to be a minimum on the potential energy surface.[27−32] There is now a broad consensus that the characteristic *ABC* triplet arises from a Fermi resonance of the ν(O−H) mode in ($_{zeolite}O-H\cdots O_{water}$) complexes with the overtone of the in-plane bending mode ($2\delta(_{zeolite}O-H\cdots O_{water})$) giving the *AB* diad and the overtone of the out-of-plane bending mode ($2\gamma(_{zeolite}O-H\cdots O_{water})$) giving the *C* band. In the *B* band, the stretch is also coupled with the second overtone of the out-of-plane bending. The additional bands around 3700 and 3550 cm^{-1} are assigned to ν(OH) modes of slightly perturbed H_2O molecules. Clusters of H_2O molecules in some cases may attain a basicity sufficiently high to abstract a proton from the zeolite lattice, giving species formally represented by $H^+(H_2O)_n$.[32,33] In this case, as involved species are characterized by a weaker H-bond, we would expect less prominent *A*, *B*, and *C* components in favor of more usual broad band not showing the characteristic Evans windows. See appendix for more details.

3.1.2 Interactions between H_2O and H-SSZ-13 at 300 K. Figure 2 presents spectra collected at increasing coverages of H_2O on a pretreated sample of H-SSZ-13. Part a presents the spectra as obtained, while part b reports difference spectra obtained using the spectrum collected before H_2O dosage as

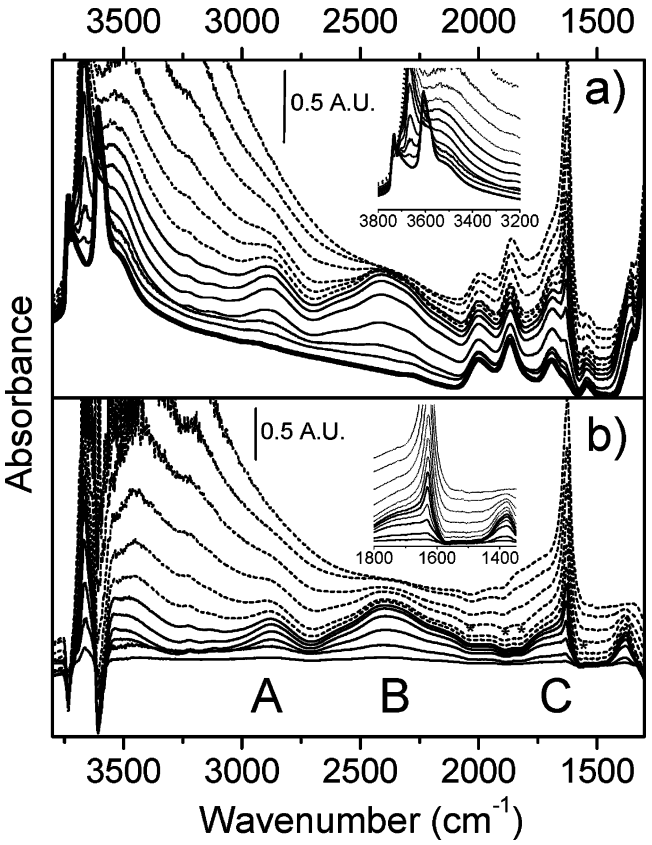

Figure 2. IR spectra of increasing doses of H_2O at 300 K on H-SSZ-13 outgassed at 773 K. (a) Full lines correspond to H_2O/H^+ ratios (x) in the 0−1 interval. Dashed curves correspond to $x > 1$. In the inset, an enlarged view of ν(OH) region is reported. (b) Reports background-subtracted spectra to clarify the formation of the *ABC* components. Asterisks indicate "false" bands because of small shifts in background bands upon interaction with H_2O, see text. In the inset, an enlarged view of δ(OH) region is reported.

background. The spectrum of the pretreated zeolite, represented by the bold curve in Figure 2a, has been thoroughly described previously,[12] and only the main features will be summarized here: (i) The absorption with a maximum around 3730 cm^{-1}: ν(OH) modes of nearly isolated silanol groups. The superimposed band with a maximum at 3710 cm^{-1} results from vibrations of vicinal silanol groups.[35] (ii) The composite band with a maximum at 3610 cm^{-1} and a shoulder at 3600 cm^{-1}: ν(OH) modes of strongly Brønsted acidic sites. (iii) Broad component around 3500 cm^{-1}: ν(OH) modes of silanol groups interacting through medium-strong H-bonds in so-called silanol nests.[35] (iv) Four groups of absorptions in the range 2000−1500 cm^{-1}: Combination and overtone modes of skeletal vibrations.

The entire set of spectra presented in Figure 2ab is divided into two subsets, displayed as solid and dashed curves. The first series of spectra is solid drawn and was collected for ratios of H_2O:Brønsted sites up to 1 and demonstrate formation of neutral H-bonded ($_{zeolite}OH\cdots O_{water}$) complexes, as illustrated in Scheme 1. The second series is dash drawn and describes formation of $H^+(H_2O)_n$ clusters formed in an excess of H_2O. The spectral details of the ν(OH) region are more evident from the inset. After having scrutinized the first subset in Figure 2a and b, the following features can be reported: A rather complex and fast-growing absorption emerges at about 3670 cm^{-1}. This absorption originates from $\nu(O-H_{b,water})$ modes of nearly unperturbed O−H bonds in H_2O, see Scheme 1.[19,20] In zeolites characterized by more spacious channels, such as the beta zeolite, the

SCHEME 1

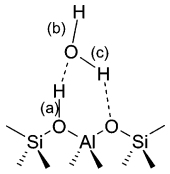

corresponding band has been observed at 3710 cm^{-1}.[19] Mihaleva et al. very recently calculated this frequency to be 3697 and 3714 cm^{-1}, on the basis of a 7T and 8T cluster, respectively.[34] 7T and 8T are clusters cut from the zeolitic framework containing seven and eight TO_4 units (T = Si or Al), respectively. The corresponding $\nu(O-H_{c,water})$ vibration (see Scheme 1), that is, water OH bonds involved in weak H-bonds to zeolite oxygens, gives a significantly broader band with a maximum around 3540 cm^{-1}. This maximum appears to shift toward lower frequencies at increasing H_2O loadings. Compared to the $\nu(O-H_{b,water})$ vibration, this absorption is downward shifted by 120 cm^{-1}. The $\nu(O-H_{c,water})$ mode was found to be 3407 cm^{-1} (7T cluster model) and 3470 cm^{-1} (8T cluster model) by Mihaleva et al.[34] The component around 3450 cm^{-1}, particularly evident from the difference spectra in Figure 2b, is related to H_2O molecules interacting with silanol groups.

The $\nu(_{zeolite}OH_a\cdots O_{water})$ mode (see Scheme 1) gives an *AB* doublet with a minimum at 2710 cm^{-1}, caused by a Fermi resonance effect between $\nu(_{zeolite}O-H_a\cdots O_{water})$ vibrations and $2\delta(_{zeolite}O-H_a\cdots O_{water})$. Note the very high frequency of the Evans window associated to the Fermi Resonance effect which is evidenced by a higher intensity of the *B* component compared to the *A* component. This feature seems to be a peculiarity of this material. To the best of our knowledge, for all other zeolites previously investigated, the intensities of the *A* and *B* components have been equivalent.[19,20] In an analogous manner, the *C* band of the *ABC* triplet is also unusually intense. The characteristic position and shape of the *ABC* triplet, together with the red-shift of the Brønsted ν(OH) mode of about 1000 cm^{-1}, point out the character of the H-bond ($_{zeolite}OH_a\cdots O_{water}$) to be fairly strong. A pronounced and asymmetric band at 1630 cm^{-1} is superimposed on the high-frequency part of the *C* component. This band, particularly evident from the inset in Figure 2b, is associated with $\delta(H_2O)$ modes of H-bonded H_2O. Upon H_2O adsorption, the zeolite framework modes (framework overtones and combination vibrations) are perturbed as testified by the appearance of negative components in the background-subtracted spectra (see asterisks in Figure 2b in the 2000−1500 cm^{-1} range).

The $\delta(_{zeolite}O-H_a\cdots O_{water})$ mode creates a broad and unresolved doublet at 1406 and 1380 cm^{-1} (the first overtone of this mode is responsible for the Evans window at 2710 cm^{-1}). Note the very high frequency of this complex absorption in comparison to other zeolites.[19,20] This behavior is consistent with a strong character of the H-bond interaction.

A final consideration is addressed to the reactivity of H_2O toward the two families of Brønsted sites. In compliance with our previous CO experiments,[12] Figure 2a clearly demonstrates that the Brønsted band, originally having its maximum at 3610 cm^{-1}, separates into two components, one at 3610 (HF) and the other at 3584 (LF) cm^{-1}. Among the two components representing the Brønsted sites, the HF component erodes faster upon H_2O adsorption as is obvious. In compliance with our previous data,[12] the sites of the HF band are easier to access for probe molecules.

The amount of H_2O introduced into the zeolite when the last spectrum of the first subset (full line curves) was collected has

SCHEME 2

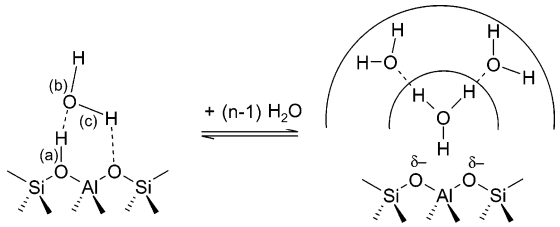

resulted in a total consumption of the Brønsted sites. Moving to subset two (dashed curves), the spectrum of the neutral hydrogen-bonded 1:1 adduct gradually erodes as clusters of H_2O are formed. Particularly clear are the erosions of the Evans window at 2710 cm^{-1}, the $\delta(_{zeolite}O-H_a\cdots O_{water})$, and the δ-$(_{zeolite}O-H_a\cdots O_{water})$ mode and the growth of a continuum absorbing from 3000 to 1300 cm^{-1}. On the basis of previous studies, it is reasonable to claim that we are no longer dealing with neutral H-bonded adducts but are entering a situation where the protons are transferred from the zeolite to H_2O clusters (see Scheme 2). The features of the spectra in Figure 2 concur well with those seen for H-beta and H-ZSM-5.[19,20] Our experimental data do not reveal any significant difference in acidic strength between the HF and LF sites.

When the highest H_2O coverage had been reached, desorption was carried out at room temperature by gradually reducing the equilibrium pressure of H_2O in the cell. The thus obtained spectra 1−6 are displayed in Figure 3, and spectrum 6 was collected after outgassing for 30 min. The low-frequency region has also been reported after background subtraction (inset of Figure 3) to elucidate the spectral modifications. A large amount of H_2O is evidently reversibly adsorbed at room temperature, even if no strong Brønsted sites are restored after the final outgassing. Spectrum 6 is characterized by the restoration of the 3670 and 3540 cm^{-1} bands. These bands were previously assigned to $\nu(O-H_{b,water})$ modes of nearly unperturbed O−H bonds in H_2O and to $\nu(O-H_{c,water})$ vibrations of H_2O involved in weak H-bonds to zeolite oxygens.[20] Moreover, we can observe the recovery of the two maxima at about 2875 and 2400 cm^{-1} (*AB* components), and of the complex absorption around 1400 cm^{-1} ($\delta(_{zeolite}O-H_a\cdots O_{water})$ mode), and the regular decrease of the band at 1632 cm^{-1} because of H_2O bending modes (inset of Figure 3). All these features indicate that a considerable amount of H_2O has been removed and the characteristic features of H_2O strongly bonded to Brønsted sites are restored, confirming the hydrophobic character of this material.

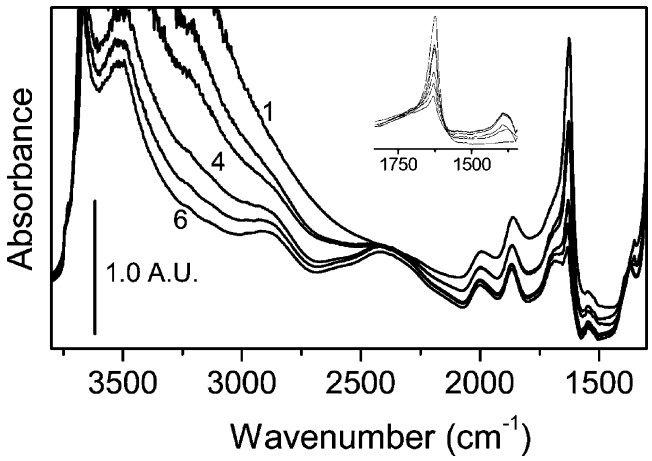

Figure 3. IR spectra taken during a desorption experiment at room temperature of H_2O adsorbed on H-SSZ-13. Curve 1, spectrum in the presence of H_2O vapor pressure; curves 2−6, effect of gradually lowering the H_2O pressure (spectrum 6 has been recorded after outgassing of 30′). In the inset, an enlarged view of δ(OH) region is reported after background subtraction.

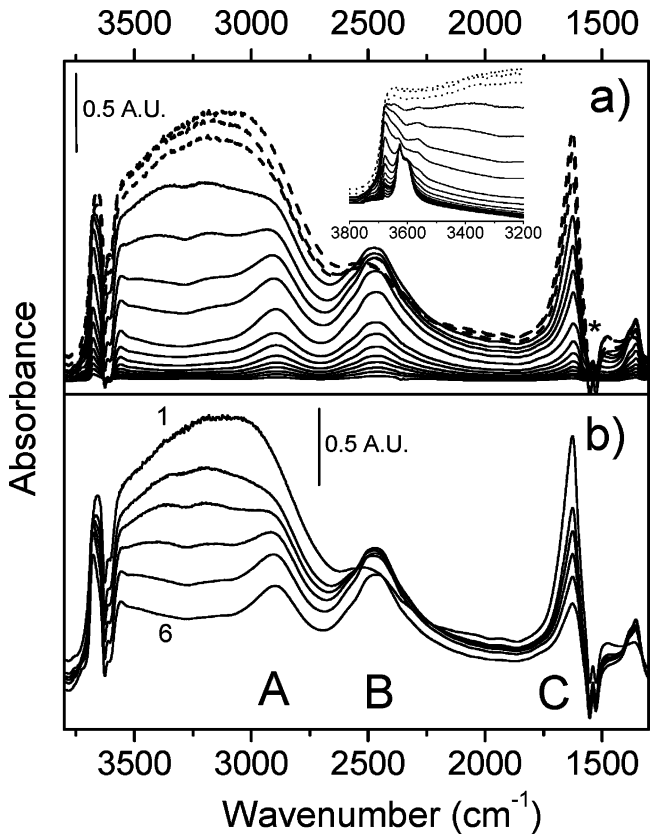

Figure 4. (a) IR spectra of increasing doses of H_2O on H-SAPO-34 at 300 K (background-subtracted spectra). Asterisks indicate "false" bands because of small shifts of background bands by interaction with H_2O. In the inset, an enlarged view of ν(OH) region is reported without background subtraction. (b) Desorption experiment at room temperature of H_2O adsorbed on H-SAPO-34. Curve 1, spectrum in the presence of H_2O vapor pressure; curves 2−6, effect of gradually lowering the H_2O pressure (spectrum 6 has been recorded after 30′ outgassing).

3.1.3 Interactions between H_2O and H-SAPO-34 at 300 K. Figure 4a presents an overview of a series of background-subtracted spectra collected at increasing coverages of H_2O on H-SAPO-34. The inset of part a reports an enlargement of the ν(OH) region as the spectra were collected (i.e., not background-subtracted). After the highest H_2O coverage had been obtained, the sample was outgassed at room temperature, and the thus obtained series of spectra (background-subtracted) is displayed in Figure 4b. Since H_2O adsorption on SAPO-34 has already been reported,[24,25] the results will be presented briefly.

When H_2O is adsorbed on the pretreated H-SAPO-34, the features that come into view can be summarized by the following points: (i) Not unexpected, the *ABC* triplet arising from $(_{zeolite}OH_a\cdots O_{water})$ H-bonding interactions is obviously present. In contrast to the parallel experiment with H-SSZ-13, the triplet is only partially eroded at high H_2O coverages (dashed curves). (ii) A complex absorption at about 3670 cm^{-1} is assigned to $\nu(O-H_{b,water})$ modes of nearly unperturbed O−H bonds in H_2O.[19,20] The corresponding $\nu(O-H_{c,water})$ vibration of water OH bonds being involved in weak H-bonds to the zeolite oxygens gives a band with a maximum around 3560 cm^{-1}. (iii) Similar to the parallel experiment with H-SSZ-13, the HF component of the Brønsted band (3627 cm^{-1}) erodes faster than the LF component (3603 cm^{-1}), pointing out the

HF sites to be the easiest ones to access for a guest molecule. (iv) The *AB* doublet is centered at 2700 cm^{-1}. Contrary to what was observed for H-SSZ-13, the *A* and *B* bands grow with equal intensities, indicating a weaker interaction with H_2O (see Appendix for a further discussion). (v) The band evolving at 1625 cm^{-1} originates from $\delta(H_2O)$ modes of H-bonded H_2O. The high-frequency component of this band grows on the *C* component. The band of the $\delta(H_2O)$ mode is twisted out of shape on the low-frequency side because of some negative components at 1552 and at 1524 cm^{-1} (see the asterisk in the figure) from combinations and overtones of framework vibrations. This phenomenon, not observed for a weak base like, for example, CO,[12] suggests that these bands selectively respond to interactions with strong ligands. (vi) A broad doublet at 1385 and 1355 cm^{-1} is assigned to a $\delta(_{zeolite}O-H_a\cdots O_{water})$ mode. At higher H_2O loadings, a band centered at 1482 cm^{-1} also appears. (vii) At medium-high coverages, we observe the formation of a complex absorption in the range 3500−3000 cm^{-1}. This is due to the presence of water add-layers and to the formation of H-bonded adducts between water and P-OH, Al-OH, and Si-OH species. (viii) Formation of protonated clustered H_2O species seems to be very limited, also at high loadings (dashed curves). (ix) Upon a prolonged pumping at 300 K (Figure 4b), also in this case a considerable fraction of adsorbed H_2O is removed and all the features of strongly adsorbed molecular H_2O are restored.

On the basis of our set of results, the most striking difference between H-SSZ-13 and H-SAPO-34 is that protonated clustered H_2O species are formed only partially on the latter material. Even at a very high H_2O loading, a considerable fraction of the Brønsted sites retain their protons as testified by the presence of the *ABC* triplet.

3.2 CH_3OH as Base for Probing the Acidity of H-SSZ-13 and H-SAPO-34 by FTIR.

3.2.1 Interactions between CH_3OH and H-SSZ-13. CH_3OH has a basicity (PA_{CH3OH} = 181.9 kcal mol^{-1}) slightly higher than H_2O (PA_{H2O} = 166.5 kcal mol^{-1}). Increasing amounts of CH_3OH was adsorbed on a pretreated H-SSZ-13, and the spectra are displayed in Figure 5a−c. Figure 5a presents the overall view over the entire set of spectra as they were recorded, part b presents an enlarged view of the OH stretching region, and part c reports the difference spectra of the low-frequency region 2100−1335 cm^{-1} covering the *C* component and the C−H bending modes. The spectrum of the pretreated zeolite prior to CH_3OH adsorption is represented by the bold curves in parts a and b. The scrutiny of the spectra in Figure 5 can be divided into two parts, one of low CH_3OH coverages (solid drawn spectra) and one related to the highest filling conditions (dashed curves). At the lowest CH_3OH coverages, the spectra are dominated by spectroscopic features which can be interpreted by considering neutral H-bonded species reported in Scheme 3. This species is typified by two hydrogen bonds: One having a medium-to-strong character with a nearly linear geometry [bond 1], the second much weaker, bent, and strongly affected by the site geometry [bond 2]. The IR spectroscopic features of the adduct depicted in Scheme 1 are dominated by the stronger H-bond (1). The maxima at about 2900, 2400, and 1705 cm^{-1} in Figure 5a constitute the *ABC* triad caused by Fermi resonance of the ν stretching and 2δ and 2γ overtones of bond 1 (Scheme 3).[36] This in turn induces the formation of two Evans windows, one at 2720 cm^{-1} and the other at 2000 cm^{-1}. Within the *ABC* triplet, the *C* component has gained intensity and actually ends up as the dominant band (see Figure 8e in the Appendix). The approximate frequency of the ν(OH) mode of

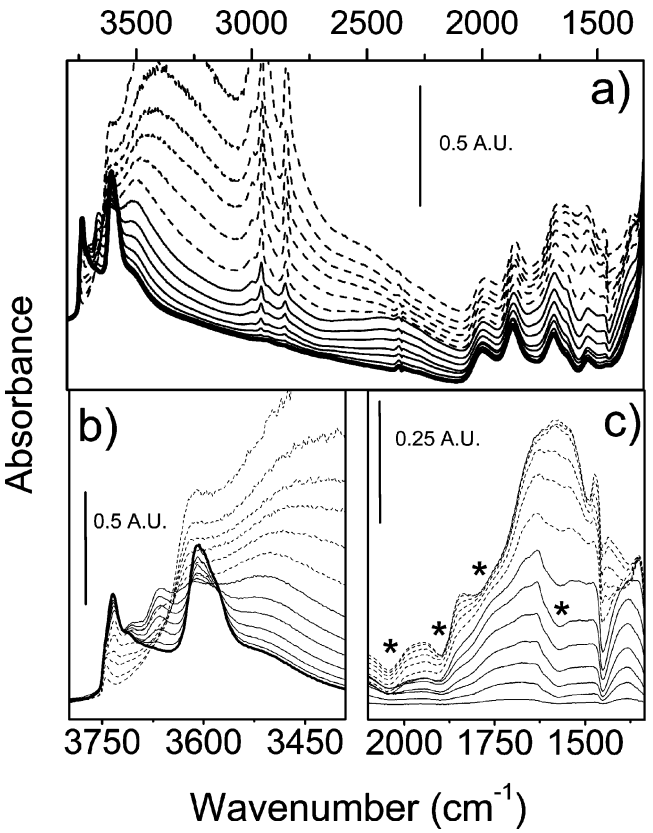

Figure 5. IR spectra of increasing doses of CH_3OH at 300 K on H-SSZ-13 outgassed at 773 K. (a) Full lines correspond to CH_3OH/H^+ ratios (x) in the 0−1 interval. Dashed curves correspond to $x > 1$. (b) Reports an enlarged view of the OH stretching region. (c) Reports background-subtracted spectra in the range 2100−1400 cm^{-1} to clarify the characteristics of the *C* component. Asterisks indicate "false" bands because of small shifts of background bands upon interaction with CH_3OH.

SCHEME 3

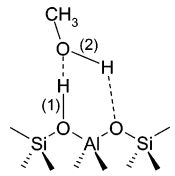

SCHEME 4

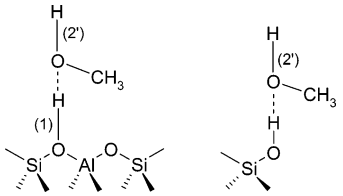

($_{zeolite}O-H\cdots O_{methanol}$)$_1$ in absence of Fermi resonance effects can be estimated to 2100 cm^{-1}. The corresponding vibration mode of bond 2 (see Scheme 3) is seen at 3500 cm^{-1}. This band grows parallel to the *ABC* triplet and confirms formation of a neutral adduct.[36] Minor features are (i) a component centered at about 3370 cm^{-1} associated with silanols groups and (ii) the growth of a band at about 3670 cm^{-1} which progressively shifts to lower wavenumbers upon increasing the CH_3OH equilibrium pressure. This band (see enlarged view in Figure 5b) can be explained in terms of nearly free ν(OH) mode of CH_3OH as reported in Scheme 4 [bond 2′]. In the presence of higher CH_3OH loadings, this component decreases in intensity

SCHEME 5

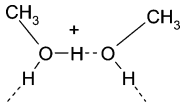

because of the formation of multilayered CH_3OH. Methyl ν-(C−H) stretching vibrations of CH_3OH at 3000, 2958, 2916, and 2854 cm^{-1} are superimposed on the *A* component. The absorptions at 3000 and 2958 cm^{-1} represent asymmetric vibrations whereas that at 2854 cm^{-1} is associated with symmetric modes of the CH_3 groups. The frequencies are slightly upward shifted compared to the vibrations of the free molecule.[37] This blue shift may be rationalized by formation of H-bonded complexes,[36] but an alternative interpretation can also be formation of methoxy groups.[38,39] This latter assignment should be accompanied by the appearance of a band representing the $\nu(O-CH_3)$ mode of the $Si-O-CH_3$ unit, but unfortunately the region where this absorption should appear is obscured by framework modes. The band at 2916 cm^{-1} is probably due to overtones of the bending $\delta(CH_3)$ mode at 1450 cm^{-1} enhanced by a Fermi resonance effect.

The evolution of the spectra in the 2000−1300 cm^{-1} range, where the *C* component is growing, shows a higher level of complexity. An enlarged view of the background-subtracted spectra is reported in Figure 5c. Four negative components, labeled with asterisks, originate from perturbative effects on the zeolitic framework induced by CH_3OH. Moreover, an additional negative band, growing at 1450 cm^{-1}, corresponds to an Evans window because of the superposition of the *C* component with a $\delta(CH_3)$ mode. This phenomenon makes it difficult to pinpoint the δ mode of bond 1 in the background-subtracted spectra. Conversely, a component at about 1380 cm^{-1} is clearly visible in Figure 5a; the δ mode of bond 2 and the γ modes of 1 and 2 are not observable as they fall in the range 1300−1000 cm^{-1}, which is obscured by framework vibrations.

When the adducts have been formed in a 1:1 ratio, further CH_3OH dosage leads to (i) a gradual intensification of the continuous background covering the whole 3500−1300 cm^{-1} interval, (ii) a nearly total erosion of silanol bands and the parallel growth of the absorption at around 3370 cm^{-1}, (iii) the weakening of the *A* component and a broadening of the *B* band, (iv) the formation of a strong absorption centered at 1600 cm^{-1}, (iv) a gradual disappearance of both the $(_{zeolite}OH\cdots O_{methanol})_1$ and $(_{zeolite}OH\cdots O_{methanol})_2$ O−H stretching modes, and (v) the region 1480−1380 cm^{-1} becomes even more complex because of the appearance of a second Evans window at 1480 cm^{-1}. This feature has been observed previously and interpreted as a direct interaction between the $\nu(OH\cdots O)$ mode and a mode directly involving the acidic hydrogen, that is, a $\delta(OH\cdots O)$ mode.[36] In practice, upon increasing the CH_3OH coverage, the spectrum evolves from a situation characteristic for medium-strong H-bonds in neutral species to a situation more characteristic for interactions found for positive and negative ions in aqueous acid or basic solutions. All these facts indicate that under these conditions, owing to the greater proton affinity of the dimers and oligomers, more ionic structures are formed (see Scheme 5). Molecular modeling simulations performed both on clusters and periodic structures confirm that in the presence of CH_3OH oligomers, protonated structures are stabilized.[6−9] It seems rather accepted, however, that the first step of the reaction is the protonation of CH_3OH; then two mechanisms have been proposed to explain formation of dimethyl ether. In the first proposed mechanism, methanol undergoes a nucleophilic attack from the zeolite to form a framework methoxy species which

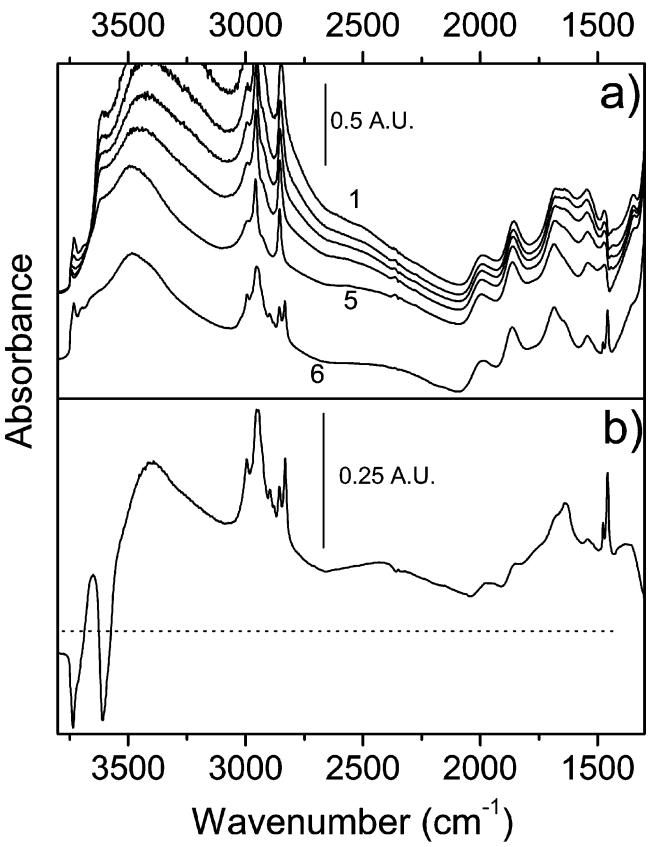

Figure 6. (a) IR spectra taken during desorption experiments of CH_3OH adsorbed on H-SSZ-13. Curve 1, spectrum in the presence of CH_3OH vapor pressure; curves 2−5, effect of gradually lowering the CH_3OH pressure at room temperature (spectrum 5 has been recorded after 30 min outgassing). Curve 6 shows the effect of a heating at 573 K for 30 min. (b) Curve 6 is reported after background subtraction.

in turn reacts with a second molecule of CH_3OH to form dimethyl ether. In the second pathway, the zeolite is not directly involved except as an acid−base "solvent" with two CH_3OH molecules directly condensing. To elucidate this aspect, we have followed the changes in the IR spectra upon removal of the fraction of reversibly adsorbed CH_3OH (outgassing at RT) and subsequent heating to 573 K for 30 min. The results are reported in Figure 6a. It is evident that CH_3OH adsorption is only partially reversible at room temperature. Indeed, even after a prolonged outgassing, all bands of CH_3OH species are still present. The entire set of strong Brønsted sites are still interacting with CH_3OH and the silanol groups are only partially restored. The final spectrum, curve 5 in Figure 6a, is characterized by well-defined *A*, *B*, and *C* components suggesting that the outgassing procedure has mainly restored unprotonated CH_3OH. After treating the sample at 573 K for 30′ (spectrum 6), some changes indicating an evolution of entrapped species can be observed. A general feature of the final spectrum, particularly clear from the background-subtracted spectrum in Figure 6b, is the very low intensity of the *A* and *B* components compared to the *C* band. Such a picture is typical for formation of particularly strong H-bond interactions, suggesting the presence of entrapped species with a higher proton affinity. When heated in acidic zeolites, CH_3OH is well-known to dehydrate to form dimethyl ether, $(CH_3)_2O$ ($PA_{(CH3)2O}$ = 189.3 kcal mol^{-1}). New bands appear in the C−H stretching and bending regions. The absorptions at 3000, 2943, and 2830 cm^{-1} can be assigned to $\nu_{sym}(CH_3)$ vibrations of H-bonded $(CH_3)_2O$ (i.e., at about 15 cm^{-1} higher than those of free molecule) accompanied by two bands at 2896 and 2860 cm^{-1}, probably associated with the

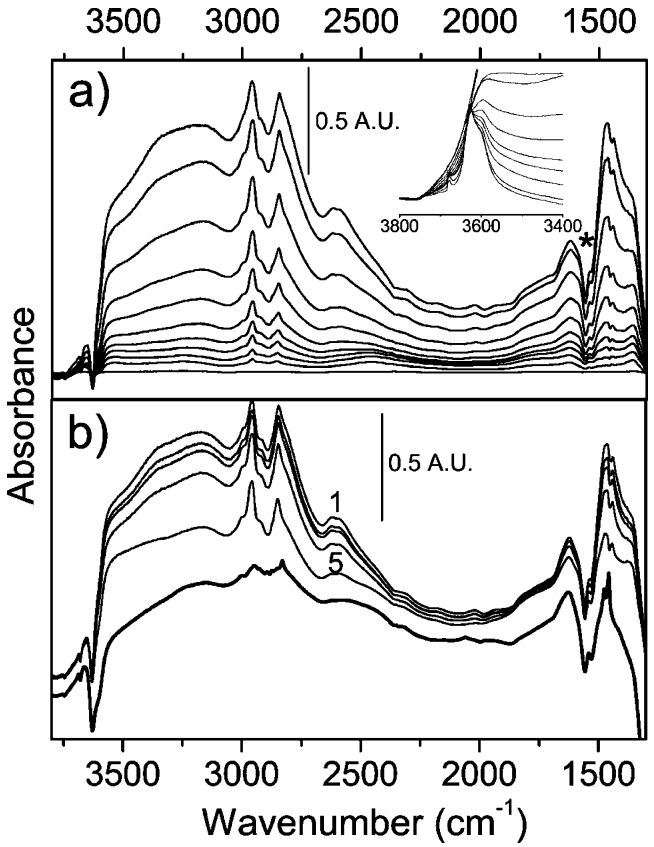

Figure 7. (a) IR spectra of increasing doses of CH_3OH on H-SAPO-34 (background-subtracted spectra). Asterisk indicates "false" bands because of small shifts of background upon interaction with CH_3OH. In the inset, an enlarged view of ν(OH) region is reported without background subtraction. (b) Desorption experiments of CH_3OH adsorbed on H-SAPO-34 (background-subtracted spectra). Curve 1, spectrum in the presence of CH_3OH vapor pressure; curves 2−5, effect of gradually lowering the CH_3OH pressure at room temperature (spectrum 5 has been recorded after 30 min outgassing). Bold curve shows the effect of a successive heating at 573 K for 30 min.

overtone bands of $\delta(CH_3)$ enhanced by Fermi resonance effects. The spectral evolution in the 2000−1300 cm^{-1} range is more complex since the formation of several negative bands makes a precise assignment more indecisive. In particular, the formation of the minima at 1570, 1490, 1471 (very narrow), and 1429 cm^{-1} can be interpreted by considering shifts of background bands and presence of Evans windows because of a resonant interaction with $\delta(OH\cdots O)$ and $\delta(CH_3)$ modes. The observed features suggest that upon heating the extensively formed dimethyl ether interacts with the acidic sites, as suggested by previous calculations.[8]

3.2.2 Interactions between CH_3OH and SAPO-34 at 300 K. An experiment similar to that described in the preceding paragraph was also conducted for H-SAPO-34, and the resulting background-subtracted spectra are presented in Figure 7. Part a shows the spectra of increasing coverages of CH_3OH on the pretreated H-SAPO-34 where the inset presents the spectra as recorded in the O−H stretching region. Part b demonstrates the effect of subsequently outgassing the sample at room temperature and then heating the system to 573 K for 30 min. The effect of progressive CH_3OH loading can briefly be summarized by the following points: (i) All Brønsted sites are eroded progressively and a broad band grows starting from 3700 cm^{-1}. The superposition of this absorption with the original ν(OH) band originates a component at 3657 cm^{-1} in the subtracted spectra. (ii) The *ABC* triad grows continuously with the *C* component gaining in intensity relative to the *A* and *B* bands. (iii) The growth of an absorption at about 3670 cm^{-1} because of the nearly free ν(OH) mode of CH_3OH. (iv) Progressive appearance of a broad absorption in the range 3500−3000 cm^{-1} because of the formation of H-bonded adducts between methanol and P−OH, Al−OH, and Si−OH species. (v) Formation of negative bands superimposed on the *C* component. The negative doublet at 1556 and 1530 cm^{-1} (see asterisk in Figure 6a) has already been singled out in the H_2O adsorption experiment and was explained in terms of modifications induced by ligands on the framework overtones.

From the overall set of data, it seems clear that even when reaching high CH_3OH loadings, no extensive deprotonation of Brønsted sites appears to take place. This somewhat unexpected result means that in the chabazite cage it is not easy to accommodate a large number of CH_3OH molecules interacting by H-bonds able to give proton transfer from the SAPO lattice.

It is evident from Figure 7b, showing the effect of outgassing, that CH_3OH adsorption is only partially reversible at RT. The final spectrum, curve 5 in Figure 7b, does not show any changes in addition to what already evidenced. The effect of the final heating to 573 K is represented by the bold curve. Not unexpected, by considering the C−H stretching and bending regions, we can conclude that a reaction has indeed occurred and $(CH_3)_2O$ has been formed. However, compared to H-SSZ-13, the impression is that in this case the phenomenon has been less extensive. Though not considered to be a rate-determining step in the CH_3OH conversion, the lower rate of $(CH_3)_2O$ formation may be interesting from a catalytically point of view.

4. Conclusions

This work represents the first experimental study of H_2O and CH_3OH adsorption on zeolite H-SSZ-13. H-SSZ-13 has a strong Brønsted acidity comparable to, or even higher than, H-ZSM-5 and H-beta. In fact, H-SSZ-13 is the only material for which the *B* component is more intense than the *A* component upon interaction with H_2O at low coverages. At high H_2O loadings, protonated H_2O clusters are prominent. The hydrophobic character of the H-SSZ-13 framework is confirmed by the reversible character of the H_2O adsorption (evacuation at RT). The final spectrum obtained after evacuating the sample at RT shows restoration of neutral H_2O strongly adsorbed on the Brønsted sites.

Importantly, H-SAPO-34 is indisputably less acidic than H-SSZ-13. H_2O protonation is a minor feature even at high coverages. The hydrophilic character of the H-SAPO-34 framework is confirmed by the low reversibility of the H_2O adsorption.

CH_3OH interacts strongly with the Brønsted sites in H-SSZ-13, and at high coverages protonated species is formed extensively. This behavior was not observed for H-SAPO-34 where only strong H-bond interactions are observed. This characteristic may be explained by considering that the shape of the chabazite cage limits the number of clustered guest CH_3OH molecules compared to the situation for H_2O. For H-SSZ-13, the nuclearity of CH_3OH clusters can be sufficiently large to extract protons, but in H-SAPO-34 larger clusters are required because of the lower acidity of the material. Upon heating, formation of $(CH_3)_2O$ has been evidenced in H-SSZ-13 even at low CH_3OH coverages. $(CH_3)_2O$ remains strongly adsorbed on the Brønsted sites.

Acknowledgment. Morton Bjørgen is grateful for financial support from the Norwegian Research Council through grant

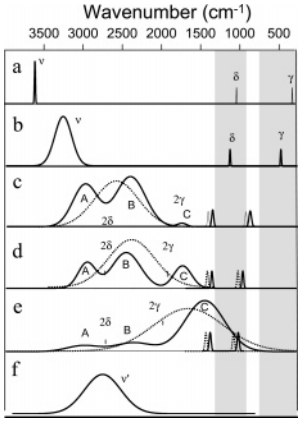

Figure 8. Qualitative representation of the IR spectroscopic features of unperturbed (a), weak (b), medium (c,d), strong A−H···B (e), and $A^-\cdots H-B^+$ (f) H-bonded complexes. The half-width of the bending modes is assumed somewhat arbitrarily to slightly increase upon increasing the hydrogen bond strength. The gray area corresponds to regions obscured by the skeletal modes of the zeolite framework. Dotted curves in parts c−e represent what should be observed in absence of Fermi resonance.

number 158552/441. Laura Regli acknowledges Regione Piemonte for financial support.

Appendix: IR Spectroscopy for Studying the Acidities of Brønsted Sites in Zeolites

The classical IR spectroscopic way to study the acidity of Brønsted sites in zeolites is to measure the perturbation of the associated vibrational modes upon interaction with bases. The method is based on the experimental observation that the formation of AH···B adducts between a Brønsted acid AH and a base B via the acid−base type reaction

$$AH + B \rightleftharpoons AH\text{----}B$$

is accompanied by a downward shift of the ν(AH) ($\Delta\bar{\nu}$) which is proportional to the reaction enthalpy. This effect, initially documented for homogeneous systems (solutions),[40] was successively verified for the heterogeneous systems such as zeolites[19,41,42] and oxides.[43]

The spectroscopy of the homogeneous AH···B systems can be outlined by briefly describing the six representative situations schematized in Figure 8: isolated AH (a), AH interacting with B through a weak H-bond (b), AH interacting with B through a H-bond of medium (c) and medium-strong (d) strength, AH interacting with B through a strong H-bond (e), and finally $A^-\cdots{}^+HB$ hydrogen-bonded ionic pairs (f), corresponding to the proton transfer. The different situations will now be discussed in more detail.

(a) Unperturbed AH. The unperturbed AH oscillator (Figure 8a) is characterized by three vibrational modes, the stretching ν and the bending modes δ and γ (in and out of the plane).

(b) AH Interacting with B through a Weak H-Bond. As a consequence of the interaction, the ν(AH) stretching undergoes a negative shift ($\Delta\bar{\nu}$) comprised in the 0−400 cm^{-1} interval and a proportional increase of the integrated intensity ($\Delta\mathbf{I}$) and of the full width at half-maximum (fwhm) (ΔFWHM) is observed. At the same time, the δ and γ bending modes shift to higher frequencies. This is schematically represented in Figure 8b. An empirical correlation exists between $\Delta\bar{\nu}$ and fwhm, as fwhm $\cong 0.75\ \Delta\nu$.[40] $\Delta\bar{\nu}$, $\Delta\mathbf{I}$, and Δfwhm are proportional to the enthalpy of formation of the H-bond.[40] The increase of the integrated intensity and of fwhm is due to anharmonic coupling between the ν mode and the low-frequency external mode ν(A···B) (in turn coupled with the thermal bath fluctuations[44]). Because of this anharmonic coupling, the ν(AH···B) mode can be better described as a continuum.

(c, d) AH Interacting with B through a H-Bond of Medium and Medium-Strong Strength. Upon formation of AH···B adducts characterized by hydrogen bonds of medium strength, $|\Delta\bar{\nu}|$ gradually increases up to 1000 cm^{-1}, with parallel increase of the fwhm and **I** (Figure 8c, d dotted curves). However, the spectroscopy of H-bonded systems of medium strength is not so simple as illustrated by the dotted curves, because the shape of the bands is deeply modified by Fermi resonance effects with 2δ and 2γ overtones (Figure 8c, d).[19] As well-known, Fermi resonance occurs between two very close vibrational levels of proper symmetry: as a consequence, the two original modes mix together and originate two different bands, each of them being a mixture of the original modes.[45] According to a simplified approach,[46] the Fermi resonance between the ν(AH···B) and the 2δ and 2γ modes of (AH···B), in medium strength hydrogen-bonded systems, modifies the profile of the ν band with appearance of up to three components (A, B, C). The simplest case is verified when the maximum of the band of the ν(AH···B) coincides with the 2δ and when the 2γ frequency is still far from the maximum of the ν(AH···B) band. In this case, the ν(AH···B) mode is split into two bands of equal intensity (A, B), while the C band appears on the extreme low-frequency flank with very low or negligible intensity (Figure 8c).

For medium-strong hydrogen bonds, $\Delta\nu$(AH···B) increases and both the 2δ and 2γ frequencies become internal to the further broadened ν(AH···B) continuum; three bands are consequently generated, named A, B, and C,[19] whose relative intensity changes gradually from $\mathbf{I}_A \cong \mathbf{I}_B \gg \mathbf{I}_C$ to $\mathbf{I}_A < \mathbf{I}_B \cong \mathbf{I}_C$ with the increase of the strength of the hydrogen bond (from medium to strong) and the decrease of the AB distance in the AH···B complex.

(e) AH Interacting with B through a Strong H-Bond. For very strong H-bonds, the interaction energy between AH and B reaches its maximum value, and correspondingly $\Delta\bar{\nu}$ also reaches its maximum ($\cong$2000−2500 cm^{-1}), Figure 8e (dotted line). In both cases, the AH···B and the $A^-\cdots{}^+HB$ structures have comparable weight in the description of the system.[19,47] Under these conditions, A and B components have low intensity, and only the C component remains as the dominating feature (full line curve in Figure 8e). This C band is very intense and broad, extending toward low frequencies. This absorption is generally modulated by a large variety of narrow Evans windows caused by direct resonant interaction with the δ (and perhaps the γ) mode and with the internal modes of the A and B moieties. Therefore, the IR spectrum of strongly hydrogen-bonded complexes is very complex, and its detailed assignment is often not well-known.

(f) The Formation of $A^-\cdots{}^+HB$ Adducts. When the proton affinity of B approaches 200 kcal mol^{-1} (such as for NH_3 and Py), the H-bond interaction between AH and B can be followed by a proton-transfer reaction leading to the formation of the anion A^- and the protonated ^+HB hydrogen-bonded pair. The probability that protonation can really occur does not depend only on the strength of the H-bond (and so, on the P.A. of the reactants), but also on the stabilization of the ionic pairs. This stabilization is due, in homogeneous conditions, to solvent effects and, in heterogeneous conditions, to the interaction with the surfaces.[48] Remembering the elementary concept that the stronger is the base B, the weaker is the hydrogen bond in the

($A^{-}\cdots^{+}HB$) pair, the IR spectroscopy of the pair (Figure 8f) becomes similar again to that of the hydrogen-bonded systems of weak-medium strength (Figure 8b). The frequency of the $\nu(BH^{+}\cdots^{-}A)$ band increases while the $\Delta\bar{\nu}$, fwhm, and **I** decrease. In Figure 8f, no attempt is made to localize the δ and γ modes, since they are heavily mixed with internal modes of BH^{+} (ring modes in PyH^{+}).[49]

References and Notes

(1) Rabo, J. A.; Pellet, R. J.; Coughlin, P. K.; Shamson, E. S. In *Zeolites as catalysts and detergent builders*; Karge, H. G., Weitkamp, J., Eds.; Elsevier: Amsterdam, 1989, pp 1−17.

(2) Stöcker, M. *Microporous Mesoporous Mater.* **1999**, *29*, 3−48.

(3) Chen, J.; Wright, P. A.; Natarajan, S.; Thomas, J. M. *Stud. Surf. Sci. Catal.* **1994**, *84*, 1731−1738.

(4) Haw, J. F.; Song, W.; Marcus, D. M., Nicholas, J. B. *Acc. Chem. Res.* **2003**, *36*, 317−326.

(5) (a) Dahl, I. M.; Kolboe, S. *J. Catal.* **1994**, *149*, 458−464. (b) Dahl, I. M.; Kolboe, S. *J. Catal.* **1996**, *161*, 304−309. (c) Mikkelsen, Ø.; Rønning, P. O.; Kolboe, S. *Microporous Mesoporous Mater.* **2000**, *40*, 95−113. (d) Arstad, B.; Kolboe, S. *Catal. Lett.* **2001**, *71*, 209−212. (e) Arstad, B.; Kolboe, S. *J. Am. Chem. Soc.* **2001**, *123*, 8137−8138. (f) Sassi, A.; Wildman, M. A.; Ahn, H. J.; Prasad, P.; Nicholas, J. B.; Haw, J. F. *J. Phys. Chem. B* **2002**, *106*, 2294−2303. (g) Bjørgen, M.; Olsbye, U.; Kolboe, S. *J. Catal.* **2003**, *215*, 30−44. (h) Haw J. F. *Phys. Chem. Chem. Phys.* **2002**, *4*, 5431−5441.

(6) Shah, R.; Gale, J. D.; Payne, C. M. *J. Phys Chem. B* **1997**, *101*, 4787−4797.

(7) Stich, I.; Gale, J. D.; Terakura, K.; Payne. C. M. *Chem. Phys. Lett.* **1998**, *283*, 402−408.

(8) Gale, J. D.; Shah, R.; Payne, M. C.; Stich, I.; Terakura, K. *Catal. Today* **1999**, *50*, 525−532.

(9) Haase, F.; Sauer, J.; Hutter, J. *Chem. Phys. Lett.* **1997**, *266*, 397−402.

(10) Hunger, M.; Wang, W. *Chem. Commun.* **2004**, 584−585.

(11) Wang, W.; Bucholz, A.; Seiler, M.; Hunger, M. *J. Am. Chem. Soc.* **2003**, *125*, 15260−15267.

(12) Bordiga, S.; Regli, L.; Cocina, D.; Lamberti, C.; Bjørgen, M.; Lillerud, K.−P. *J. Phys. Chem. B* **2005**, *109*, 2779−2784.

(13) Smith, L. J.; Davidson, A.; Cheetham, A. K. *Catal. Lett.* **1997**, *49*, 143−146.

(14) Lok, M. B.; Messina, C. A.; Patton, R. L.; Gajek, R. T.; Cannan, T. R.; Flanigen, E. M. U.S. Patent 4 440 871, examples 35 and 36, 1984.

(15) Zones, S. I. U.S. Patent 4 544 538, 1985. Zones, S. I., private communication.

(16) Jentys, A.; Warecka, G.; Derewinski, M.; Lercher, J. A. *J. Phys. Chem.* **1989**, *93*, 4837−4843.

(17) Parker, L. M.; Bibby, D. M.; Burns, G. R. *Zeolites* **1991**, *11*, 293−297.

(18) Wakabayashi, F.; Kondo, J. N.; Domen, K.; Hirose, C. *J. Phys. Chem.* **1996**, *100*, 1442−1444.

(19) Pazé, C.; Bordiga, S.; Lamberti, C.; Salvalaggio, M.; Zecchina, A.; Belussi, G. *J. Phys. Chem. B* **1997**, *101*, 4740−4751.

(20) Zecchina, A.; Geobaldo, F.; Spoto, G.; Bordiga, S.; Ricchiardi, G.; Buzzoni, R.; Petrini, G. *J. Phys. Chem.* **1996**, *100*, 16584−16599.

(21) Kondo, J. N.; Iizuka, M.; Domen, K. *Langmuir* **1997**, *13*, 747−750.

(22) Domen, K.; Fujino, T.; Wada, A.; Hirose, C.; Kano, S. S. *Microporous Mesoporous Mater.* **1998**, *21*, 673−678.

(23) Lee, B.; Kondo, J. N.; Domen, K.; Wakabayashi, F. *J. Mol. Catal. A: Chem.* **1999**, *137*, 269−272.

(24) Smith, L. J.; Cheetham, A. K.; Morris, R. E.; Marchese, L.; Thomas, J. M.; Wright, P. A.; Chen, J. *Science* **1996**, *271*, 799−801.

(25) Marchese, L.; Chen, J.; Wright, P. A.; Thomas; J. M. *J. Phys. Chem.* **1993**, *97*, 8109−8112.

(26) Pelmenschikov, A. G.; van Santen, R. A. *J. Phys. Chem.* **1993**, *97*, 10678−10680.

(27) Sauer, J.; Ugliengo, P.; Garrone, E.; Saunders: V. R. *Chem. Rev.* **1994**. *94*, 2095−2160.

(28) Krossner, M.; Sauer, J. *J. Phys. Chem.* **1996**, *100*, 6199−6211.

(29) Gale, J. D. *Top. Catal.* **1996**, *3*, 169−194.

(30) Tajima, N.; Taketsugu, T.; Hirao, K. *Chem. Phys.* **1997**, *218*, 257−265.

(31) Zygmunt, S. A.; Mueller, R. M.; Curtiss, L. A.; Iton, L. E.; *J. Mol. Struct. (THEOCHEM)* **1998**, *430*, 9−16.

(32) Nusterer, E.; Blöchl, P. E.; Schwarz, K. *Chem. Phys. Lett.* **1996**, *253*, 448−455.

(33) Termath, V.; Haase, F.; Sauer, J.; Hutter, J.; Parrinello, M. *J. Am. Chem. Soc.* **1998**, *120*, 8512−8516.

(34) Mihaleva, V. V.; van Santen, R. A.; Jansen A. P. J. *J. Chem. Phys.* **2004**, *120*, 9212−9221.

(35) Bordiga, S.; Ugliengo, P.; Damin, A.; Lamberti, C.; Spoto, G.; Spanò, G.; Buzzoni, R.; Dalloro, L.; Rivetti, L. *Top. Catal.* **2001**, *15*, 43−52.

(36) Zecchina, A.; Bordiga, S.; Spoto, G.; Scarano, D.; Spanò, G.; Geobaldo, F. *J. Chem. Soc., Faraday Trans.* **1996**, *9*, 4863−4875.

(37) Coltup, N. B.; Daly, L. H.; Wiberley, S. E. *Introduction to infrared and Raman Spectroscopy*; Academic Press: London, 1995; p 220.

(38) Pelmenshikov, A. G.; Morosi, G.; Gamba, A.; Zecchina, A.; Bordiga, S.; Paukshtis, E. A. *J. Phys. Chem.* **1993**, *97*, 11979−11986.

(39) Forester, T. R.; Howe, R. F. *J. Am. Chem. Soc.* **1987**, *109*, 5076−5082.

(40) Pimentel, G. C.; McClellan, A. L. In *The Hydrogen bond*; Pauling, L. Ed.; San Francisco, 1960.

(41) Kubelková, L.; Beran, S.; Lercher, J. A. *Zeolites* **1989**, *9*, 539−543.

(42) Zecchina, A.; Buzzoni, R.; Bordiga, S.; Geobaldo, F.; Scarano, D.; Ricciardi, G.; Spoto, G. *Stud. Surf. Sci. Catal.* **1995**, *97*, 213−222.

(43) (a) Galkin, G. A.; Kiselev, A. V.; Lygin, V. I. *Trans. Faraday Soc.* **1964**, *60*, 431−439. (b) Kiselev, A. V. *Surf. Sci.* **1965**, *3*, 292−293.

(44) Bratos, S. *J. Chem. Phys.* **1975**, *63*, 3499−3509.

(45) Herzberg, G. *Molecular Spectra and Molecular Structure*, F. R. S.-II. *Infrared and Raman Spectra of Polyatomic Molecules*; D. Van Nostrand Company, Inc.: New York, 1945; p 216.

(46) Odinokov, S. E.; Jogansen, A. V. *Spetrochim. Acta, Part A* **1972**, *28*, 2343−2350.

(47) Böhner, U.; Zundel, G. *J. Phys. Chem.* **1986**, *90*, 964−973.

(48) (a) Parrillo, D. J.; Gorte, R. J. *J. Phys. Chem.* **1993**, *97*, 8786−8792. (b) Parrillo, D. J.; Gorte, R. J.; Farneth, W. E. *J. Am. Chem. Soc.* **1993**, *115*, 12441−12445.

(49) Buzzoni, R.; Bordiga, S.; Ricchiardi, G.; Lamberti, C.; Zecchina, A.; Bellussi, G. *Langmuir* **1996**, *12*, 930−940.